Influence of variable side-stay geometry on the shimmy dynamics of an aircraft dual-wheel main landing dear

Chris Howcroft[*], Bernd Krauskopf[†], Mark H. Lowenberg[‡], and Simon A. Neild[§]

August 2012

Abstract

Commercial aircraft are designed to fly but also need to operate safely and efficiently as vehicles on the ground. During taxiing, take-off and landing procedures the landing gears of an aircraft must operate reliably over a wide range of forward velocities and vertical loads. Specifically, they must maintain straight rolling under a wide variety of operating conditions. It is well known, however, that under certain conditions the wheels of an aircraft landing gear may display unwanted oscillations — referred to as shimmy oscillations — during ground manoeuvres. Such oscillations are highly unwanted from a safety and a ride-comfort perspective.

In this paper we conduct a study into the occurrence of shimmy oscillations in a main landing gear (MLG) of a typical mid-size passenger aircraft. Such a gear is characterised by a main strut attached to the wing spar with a side-stay that connects the main strut to an attachment point closer to the fuselage center line. Nonlinear equations of motion are developed for the specific case of a two-wheeled MLG configuration, and allow for large angle deflections within the geometrical framework of the system. The dynamics of the MLG are expressed in terms of three degrees of freedom: torsional motion, in-plane motion and out-of-plane motion (with respect to the side-stay plane). These are modelled by oscillators that are coupled directly through the geometric configuration of the system as well as through the tyre/ground interface, which is modelled here by the von Schlippe stretched string approximation of the tyre dynamics. The mathematical model is fully parameterised and parameters are chosen to represent a generic (rather than a specific) landing gear. In particular, the positions of the attachment points are fully parameterised so that any orientation of the side-stay plane can be considered. The occurrence of shimmy oscillations is studied by means of a two-parameter bifurcation analysis of the system in terms of the forward velocity of the aircraft and the vertical force acting on the gear. The effect of a changing side-stay plane orientation angle on the bifurcation diagram is investigated. We present a consistent picture that captures the transition of the two-parameter bifurcation diagram as a function of this angle, with a considerable complexity of regions of different types of shimmy oscillations for intermediate and realistic side-stay plane orientations. In particular, we find a region of tri-stability in which stable torsional, in-plane and out of plane shimmy oscillations coexist.

[*]Department of Engineering Mathematics, University of Bristol, University Walk, Bristol BS8 1TR, United Kingdom (c.howcroft@bristol.ac.uk).

[†]Department of Mathematics, The University of Auckland, Private Bag 92019, Auckland 1142, New Zealand (b.krauskopf@auckland.ac.nz).

[‡]Department of Aerospace Engineering, University of Bristol, University Walk, Bristol BS8 1TR, United Kingdom (m.lowenberg@bristol.ac.uk).

[§]Department of Mechanical Engineering, University of Bristol, Queen's Building, University Walk, Bristol BS8 1TR, United Kingdom (simon.neild@bristol.ac.uk)

1 Introduction

The technical term shimmy is generally used to describe the self-sustained oscillations of a rolling system, which represent a relatively well-studied problem in engineering. Typical examples of shimmy with which the reader may be familiar range from the weaving of a towed trailer at high speeds to the sudden oscillation of a loose trolley wheel. The phenomenon first began to attract research interest in connection with the undesirable oscillation of the steering mechanism of early automobiles. These vehicles shared the common design elements of a single front axle rigidly connected to the front wheels, and the severity of the problem increased further with the development of balloon tyres and front wheel brakes. The first major contribution towards an understanding of shimmy dynamics was provided in 1925 by Broulheit [5], who recognised the role of tyre flexibility and side slip in the shimmy mechanism. Furthermore, he also argued that the energy required to drive shimmy oscillations was made available through the dynamics of the tyres. This work is particularly significant as such considerations still form the basis of shimmy research today. Around the same time, de Lavard formulated a theory of shimmy involving a system with rigid tyres and in 1927 published research showing shimmy oscillations in such a system [26, 27]. This emphasised the importance of structural flexibility in the shimmy mechanism — a conclusion supported in the work of Moreland [20]. In de Lavaud's later work [28] he goes on to highlight the possible advantages of independent front wheel suspensions. This modification later proved very effective, and the development of such suspension configurations in the early 1930s almost entirely eliminated the problem of automotive shimmy. However, around the same time the development of tricycle landing gear configurations on aircraft resulted in a substantial increase in incidences of nose landing gear shimmy, consequently shifting research interest from automotive to aircraft applications. In fact aircraft shimmy has largely dominated the literature ever since, and examples of such shimmy events in aircraft can be seen in references [1, 13, 15, 19, 34]. For further information we direct the reader to the survey papers of Dengler [9] and Pritchard [21] as entry points to the literature.

Of particular significance to our research is the consideration of relevant system nonlinearities in the shimmy mechanism. The importance of these effects was realised by Temple in his 1941 paper [30] in which he considers the problem of large amplitude shimmy. There he points out that such oscillations may be excited by relatively small perturbations and that the resulting shimmy modes are highly nonlinear, meaning that their stability may not be predicted with linear methods. Similarly Rotta [25] states that linear analysis techniques can provide insight into the small amplitude stability of a system but that the determination of quantities such as shimmy amplitudes requires the consideration of system nonlinearities. Since these early works a multitude of modelling efforts have taken such nonlinearities into account. References [2, 4, 10, 17, 37] consider a range of effects, including Coulomb friction, torsional freeplay, spring hardening, nonlinear tyre modelling, oleo damping and impact dynamics.

One way of studying the effects of such nonlinearities on the dynamics of an aircraft landing gear system is to perform a bifurcation study of a suitable mathematical model by means of the numerical continuation of solutions and their bifurcations. This dynamical systems approach has been used in a relatively small number of aeronautical application contexts, which include the bifurcation study of the flight dynamics of different types of aircraft [3, 6, 18] and, more recently, aircraft ground dynamics [7, 8, 24, 23, 22, 31, 32, 33]. The usefulness of continuation methods in an industrial design context is discussed for the prediction of the low-speed ground turning of a civil aircraft in [7], and for medium-speed aircraft ground manoeuvres in [8] . The stability of aircraft turning on the ground under constant thrust conditions is considered in [24, 23], and canard orbits in the loss of lateral turning stability are the subject of [22]. Of particular interest for the study presented here is the work in [31, 32, 33] on shimmy oscillations in an aircraft nose landing gear (NLG). The papers [31, 32] present a bifurcation study of shimmy oscillations of an NLG with a single wheel in terms of the velocity of the aircraft and the loading force on the gear. This work was expanded in [33] to a dual-wheel configuration, which allowed for the assessment of the effects of gyroscopic forces and axle width on shimmy behaviour of the NLG.

In this paper we perform a bifurcation analysis of shimmy oscillations in a dual-wheel aircraft main landing gear (MLG). A key new aspect of this study — compared to an NLG as studied in [31, 32, 33] — is that the side-stay, which fixes the gear in the downlocked position, may be mounted in different orientations. For a typical NLG the sidestay plane (spanned by the side-stay and the main strut of the gear) does not have a lateral component (with respect to the direction of travel of the aircraft). The side-stay of a MLG on a typical civil

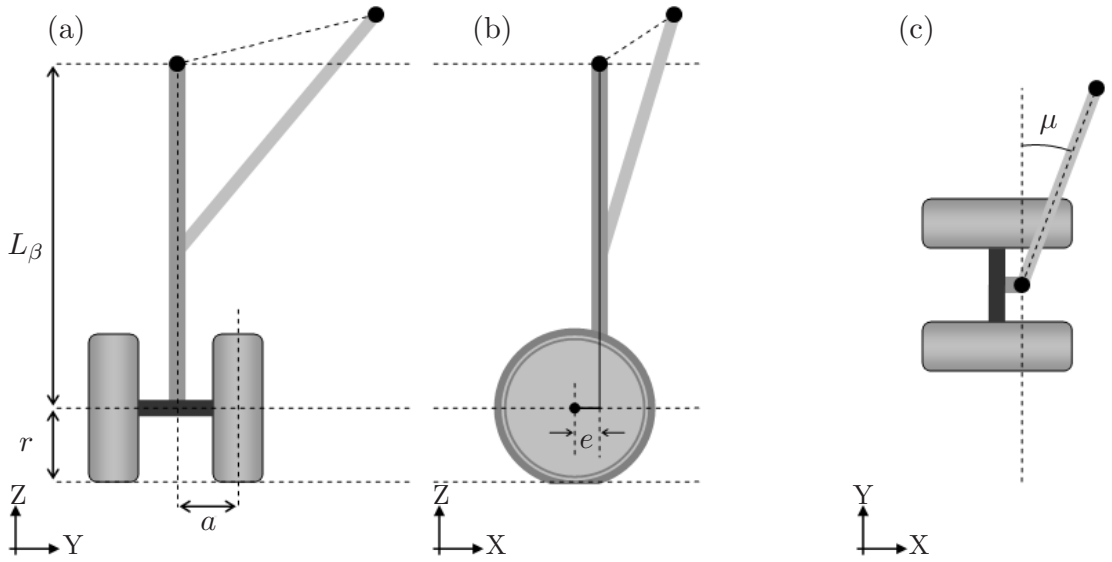

Figure 1: Parameterisation of a typical dual-wheel MLG geometry. Global co-ordinates shown are aligned with X in the forward direction, Y to port and Z pointing vertically upwards. For simplicity the gear is shown here for the zero-rake angle case and, therefore, the main strut is aligned with the Z axis.

aircraft, on the other hand, is mounted largely laterally, with its attachment point closer to the center of the fuselage; see figure 1. Furthermore the exact orientation of the side-stay plane differs from aircraft to aircraft and as a result, the geometric complexity of a MLG is generally greater than that of a NLG.

To study MLG oscillations we introduce a mathematical model that describes the motion of the system in terms of three degrees of freedom: torsional rotation about the strut axis, in-plane motion in the side-stay plane, and out-of-plane motion perpendicular to the side-stay plane. We refer to these as the three basic modes of oscillation of the MLG, and they are modelled as damped oscillators, which are coupled geometrically via the MLG structure as well as via the forces that arise at the tyre/ground interface. With an appropriate tyre model of the contact dynamics of the dual wheel, we obtain a seven-dimensional system of first-order ODEs for the dynamics of the MLG. The model is fully parameterised so that it can represent any given MLG geometry. In particular, we are able to study the sensitivity of the system to the orientation of the side-stay plane, which strongly influences the geometric coupling between the three basic modes. More specifically, for suitably chosen values of the side-stay orientation angle we present bifurcation diagrams in the parameter plane of aircraft velocity and vertical load on the MLG. Each such two-parameter bifurcation diagram is organised by curves of Hopf bifurcations, saddle-node bifurcations of periodic orbits and torus bifurcations. They bound parameter regions in which one finds different types of shimmy oscillations of the system, which are characterised by the dominance of one or more of the three basic modes of oscillation. We find a greatly increased complexity of (often coexisting) shimmy oscillations for intermediate and realistic values of the side-stay orientation angle.

The paper is organised as follows. In section 2 we present the model of the MLG, which characterises the motion of the system in terms of three oscillatory modes and the tyre contact dynamics. In section 3 this model is used to determine the dynamics for the simplest geometric case of a side-stay that is perpendicular to the direction of travel and has an attachment point level with that of the main strut. The effect on the bifurcation diagram of changing the side-stay orientation angle is then studied in section 4. Finally, in section 5 we draw some conclusions and point to future work.

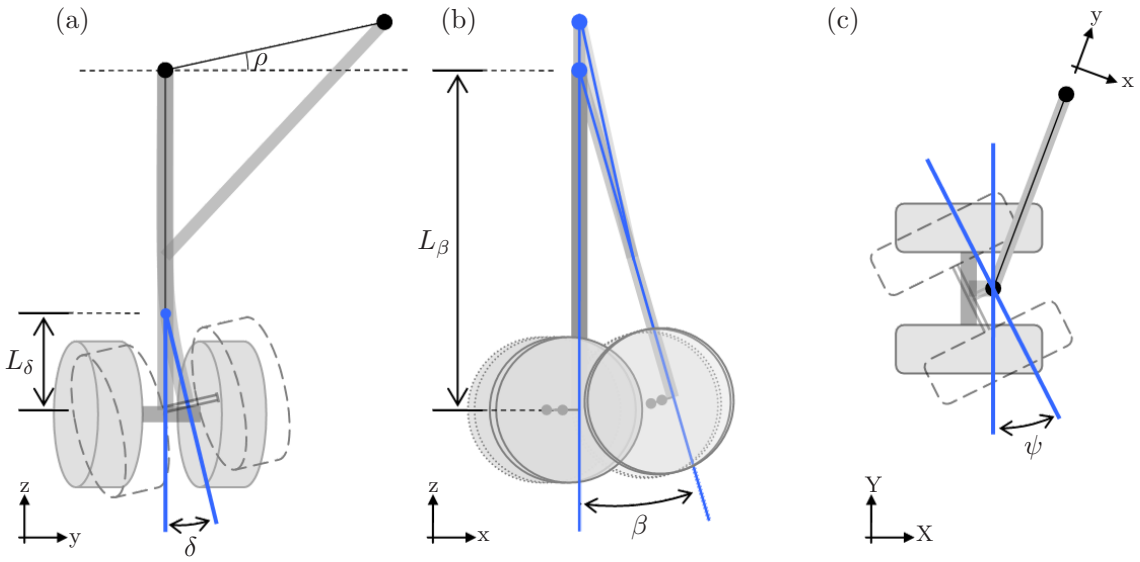

Figure 2: The dynamics of the MLG are expressed by the mode δ in the side-stay plane (a), the mode β out of the side-stay plane (b), and the torsional mode ψ (c). Due to the existence of the side-stay, in-plane bending of the main strut is approximated as an angular deflection about a point at distance L_δ above the axle. Local coordinates $(\mathrm{x}, \mathrm{y}, \mathrm{z})$ are defined with z aligned with the main strut, x perpendicular to the main strut and side-stay, and y chosen to complete the right-handed coordinate system. For the zero rake angle case shown here one has $\mathrm{z} = \mathrm{Z}$.

2 Vector Model of a main landing gear

For our study we consider a typical MLG dual-wheel geometry, consisting of a main strut, side-stay and axle assembly characterising the MLG design of a wide array of aircraft. A representation of this geometry is shown in figure 1. We use L_β to denote the length of the gear from the wheel axle centre to the top of the main strut as indicated, r is the radius of the tyres, a their separation from the axle centre, and e the caster length, expressing the shortest distance between the main strut and wheel axle center line. We allow the MLG to have a rake angle ϕ_s, defined as the angle between the main strut and the vertical Z-axis. This angle is shown in figure 3; for clarity we initially consider the zero rake angle case in figure 1.

An important feature of our model is that the orientation of the attachment points is fully parameterised by the angles μ and ρ. This parameterisation adds significant flexibility to our model, as in most cases the difference between aircraft MLG designs can be characterised simply as a change of this side-stay geometry. We use ρ to describe the inclination of these points (as shown in figure 2) and μ to describe the orientation of their projection in the (X, Y) plane, taken from the Y axis (shown in figure 1). The MLG may even approach the configuration of a NLG as the parameter μ approaches $\pm 90^\circ$, with the side-stay becoming the NLG drag-stay; compare with [31].

The presence of a side-stay in the system suggests a suitable treatment of the dynamics expressed in terms of three degrees of freedom that are represented by three basic modes of oscillation, two of which are defined with respect to the side-stay orientation. We refer to them as the torsional mode ψ, the in-plane mode δ in the side-stay plane (spanned by the main strut and side-stay), and the out-of-plane mode β in the direction perpendicular to the side-stay plane. In the formulation we consistently first apply ψ, δ and then β. The three basic modes are shown in figure 2 for the zero rake angle case; for non-zero rake angles the orientation of these modes is given by the vectors in figure 5. Note that in figure 2 we use the local co-ordinates (x, y, z) to define the orientation of the modes δ and β. Rotational vectors representing the orientation of these modes are also given in figure 5.

By considering the dynamics of each of these modes (as well as an appropriate representation of the tyre

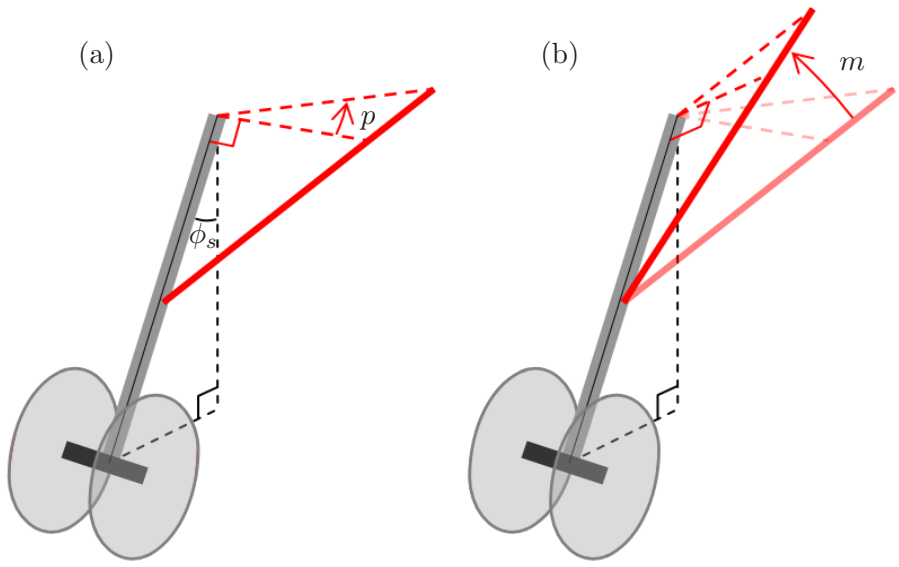

Figure 3: Angles m and p used to parameterise side-stay orientation, which are aligned relative to the main strut rather than the global coordinate system.

dynamics; see section 2.2) we will build up a model of the MLG system. To facilitate the construction of this model we adopt a vector notation throughout. In particular, this allows us to resolve any forces affecting the gear into moments acting on the three basic modes, with the resultant terms expressed in a compact form without the necessity of providing simplifying assumptions. The vector formulation also casts the system in a more flexible framework, allowing for an easy incorporation of extra forces as well as changes to the geometry. This extra flexibility will prove particularly useful when we investigate the effects of changing the side-stay orientation angle in section 4.

2.1 Equations of Motion

To begin with, we consider the free dynamics of the MLG system, that is, the behaviour of the gear when freely suspended above the ground by its attachment points. We construct expressions representing the dynamics of each of the three degrees of freedom of this free system by applying Newton's second law to each in turn. As in [31] for a NLG, our starting point is that the corresponding three basic modes couple though the dynamics of the tyre, where we neglect further effects such as the gyroscopic coupling produced by the spinning wheels. We are, therefore, able to validate our model against existing results as well as gauge the coupling effects of the variable side-stay geometry in isolation. Further geometric coupling occurs between the three basic modes when the attachment point orientation is varied. To express this we introduce the angles p and m, giving the orientation of the attachment points relative to the (y, z)-plane (shown in figure 3), rather than the global coordinate system. Note that these angles coincide with ρ and μ for the zero rake angle case ($\phi_s = 0$). From the angles p and m we can see that independence of the modes ψ and β implies that $p = 0$ (for $p \neq 0$ any β motion of the system about the attachment points will also result in a twisting of the gear at the wheel axle). For non-zero p we may write expressions for each of the modes as:

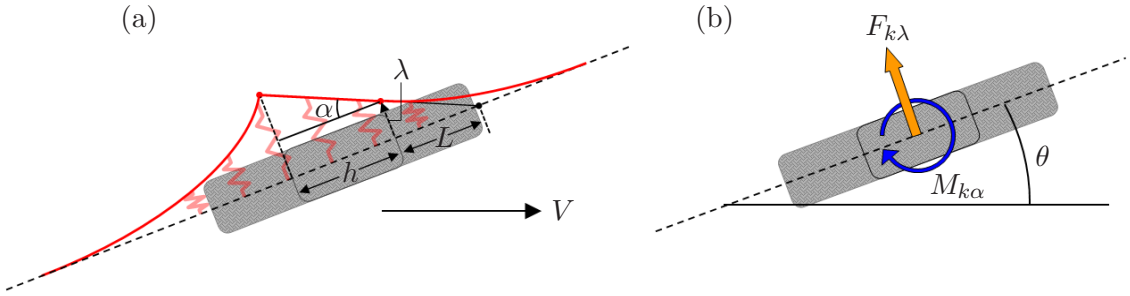

Figure 4: Panel (a) shows the von Schlippe straight line tangency assumption of the contact patch shape and resultant slip angle α describing its orientation, and in panel (b) the angle α is used to calculate tyre forces $F_{k\lambda}$ and $M_{k\alpha}$ acting on the system.

$$I_\psi\ddot{\psi} + c_\psi(\dot{\psi} + \dot{\beta}\sin p) + k_\psi(\psi + \beta\sin p) - M_\psi(\psi,\delta,\beta,\lambda) = 0\,, \tag{1}$$

$$I_\delta\ddot{\delta} + c_\delta\dot{\delta} + k_\delta\delta - M_\delta(\psi,\delta,\beta,\lambda) = 0\,, \tag{2}$$

$$\begin{aligned} I_\beta\ddot{\beta}\cos p + \Big[\ (c_\beta + c_\psi\sin^2 p)\dot{\beta} + (c_\psi\sin p)\dot{\psi}\ \Big] \\ + \Big[\ (k_\beta + k_\psi\sin^2 p)\beta + (k_\psi\sin p)\psi\ \Big] - M_\beta(\psi,\delta,\beta,\lambda) = 0\,, \end{aligned} \tag{3}$$

where the parameters $I_{\psi,\delta,\beta}$, $c_{\psi,\delta,\beta}$ and $k_{\psi,\delta,\beta}$ represent the inertial, damping and stiffness values of their respective modes, and the terms $M_{\psi,\delta,\beta}$ denote moment forces acting on the system, resolved into the three modal directions. Furthermore, λ is the lateral deflection of the tyres, calculated from an appropriate tyre model that is introduced next.

2.2 Tyre Model

Having modelled the behaviour of the free system (1)–(3) we now wish to capture the full dynamics of the MLG by considering the tyre-ground interface and associated tyre dynamics. These tyre dynamics are necessary for the appearance of shimmy oscillation, extracting energy from the forward motion of the system and feeding it into the three structural modes [36]. They also produce additional coupling between the modes. Hence, to fully model the MLG system we must introduce an appropriate tyre model. For this study we use a stretched string approximation of the tyre dynamics known as the von Schlippe tyre model [35]. This model is one of several stretched string tyre variant, and it has been regarded in the literature as generally consistent with experimental data. For our system this model is adapted to the dual-wheel case and takes the form,

$$\dot{\lambda} + \frac{V}{L}\lambda + V\mathbf{u}_{\lambda,x} + \frac{1}{2}\left(\mathbf{V}_{LCF} + \mathbf{V}_{RCF}\right)\cdot\mathbf{u}_\lambda = 0\,, \tag{4}$$

where λ is the lateral deformation of the tyres, V is the forward velocity of the system (aligned with the X-direction), and L is the relaxation length of the tyres; here $\mathbf{u}_{\lambda\,x}$ denotes the X component of the lateral tyre vector $\mathbf{u}_\lambda$; see section 2.3. The terms $V_{LCF}\cdot\mathbf{u}_\lambda$ and $V_{RCF}\cdot\mathbf{u}_\lambda$ give the lateral velocity of the left and right wheels respectively, where

$$\begin{aligned} \mathbf{V}_{LCF} &= \mathbf{u}_\psi\times(\mathbf{P}_{LCF}-\mathbf{P}_\psi)\,\dot{\psi} + \mathbf{u}_\delta\times(\mathbf{P}_{LCF}-\mathbf{P}_\delta)\,\dot{\delta} + \mathbf{u}_\beta\times(\mathbf{P}_{LCF}-\mathbf{P}_\beta)\,\dot{\beta}\ , \\ \mathbf{V}_{RCF} &= \mathbf{u}_\psi\times(\mathbf{P}_{RCF}-\mathbf{P}_\psi)\,\dot{\psi} + \mathbf{u}_\delta\times(\mathbf{P}_{RCF}-\mathbf{P}_\delta)\,\dot{\delta} + \mathbf{u}_\beta\times(\mathbf{P}_{RCF}-\mathbf{P}_\beta)\,\dot{\beta}\,. \end{aligned}$$

Again, these vectors are defined later in section 2.3.

With this tyre model, we may use the lateral deflection λ to approximate the slip angle α of the contact region, which we assume to have length h. This is based on the assumption that within this region the deflection of the tyre, given by the red line in figure 4, may be represented by a straight line continuing smoothly from the front of the contact patch. This allows the orientation of this region to be represented by the angle α, which may be written as

$$\alpha = \tan^{-1}\left(\frac{\lambda}{L}\right).$$

Knowledge of this angle allows us to model the reaction forces produced at the tyres. They consist of a lateral reaction force $F_{k\lambda}$ and a self aligning moment $M_{k\alpha}$; see figure 4. References [29] and [31] provide expressions that may be used in approximating these terms; they are

$$F_{k\lambda} = k_\lambda \tan^{-1}(7.0\tan\alpha)\cos(0.95\tan^{-1}(7.0\tan\alpha))F_z\,, \tag{5}$$

$$M_{k\alpha} = \begin{cases} k_\alpha\ \alpha_m/\pi\ \sin(\pi\alpha/\alpha_m)F_z & \text{if} |\alpha| \leq \alpha_m \\ 0 & \text{if} |\alpha| > \alpha_m \end{cases}, \tag{6}$$

where k_λ and k_α are the lateral and torsional stiffness of the tyre respectively, F_z is the vertical force acting on the system, and α_m is the maximum slip angle beyond which we take $M_{k\alpha} = 0$.

2.3 Derivation of Force Terms

We must now determine expressions for the moments acting in each of the three modal directions, given by the terms $M_{\psi,\delta,\beta}$ in equations (1)–(3). These forces and moments acting on the system are a consequence of the weight of the aircraft and the MLG, the forces produced at the tyre-ground interface, and the rolling stiffness of the dual-wheel configuration. To model their effects on the system we must resolve the moments they create in each of the modal directions. In general, these moments take the form $\mathbf{P}\times\mathbf{F}\cdot\mathbf{u}$ where $\mathbf{F}$ is the applied force, $\mathbf{P}$ the vector of the appropriate moment arm and $\mathbf{u}$ the unit vector expressing the orientation of the mode in question. We therefore define a series of position vectors for the MLG representing important geometric points as well as the points of force application; they are displayed graphically in figure 5 and are given as:

$$\mathbf{P}_\delta = (0,0,0)\,,$$
$$\mathbf{P}_\beta = R(\mathbf{u}_\beta,\beta)R(-\mathbf{e}_{_Y},\phi_0)(0,0,L_\beta - L_\delta)\,,$$
$$\mathbf{P}_0 = R(\mathbf{u}_\beta,\beta)R(\mathbf{u}_{\delta 0},\delta)R(-\mathbf{e}_{_Y},\phi_0)(0,0,-L_\delta)\,,$$
$$\mathbf{P}_L = R(\mathbf{u}_\beta,\beta)R(\mathbf{u}_{\delta 0},\delta)R(\mathbf{u}_{\psi 0},\psi_s)R(-\mathbf{e}_{_Y},\phi_0)(-e,a,-L_\delta)\,,$$
$$\mathbf{P}_R = R(\mathbf{u}_\beta,\beta)R(\mathbf{u}_{\delta 0},\delta)R(\mathbf{u}_{\psi 0},\psi_s)R(-\mathbf{e}_{_Y},\phi_0)(-e,-a,-L_\delta)\,,$$
$$\mathbf{P}_{LC} = \mathbf{P}_L + r\,\mathbf{u}_r\,,$$
$$\mathbf{P}_{RC} = \mathbf{P}_R + r\,\mathbf{u}_r\,,$$
$$\mathbf{P}_{LCF} = \mathbf{P}_L + 1/2\,h\,\mathbf{u}_f\,,$$
$$\mathbf{P}_{RCF} = \mathbf{P}_R + 1/2\,h\,\mathbf{u}_f\,,$$

where $R(\mathbf{v},\theta)$ denotes the rotation matrix corresponding to a rotation of θ radians about the vector $\mathbf{v}$. Moreover, $\mathbf{e}_{_X}$, $\mathbf{e}_{_Y}$, $\mathbf{e}_{_Z}$ are unit vectors in the X, Y and Z global directions, respectively, ϕ_s is the (dynamically changing) rake angle of the MLG, and ϕ_0 is its static value for $(\psi,\delta,\beta) = \mathbf{0}$.

We also define the following vectors describing the orientation of the MLG modes, as well as the orientation of various constituent parts of the system; these are shown in figure 5 and are written in the global reference

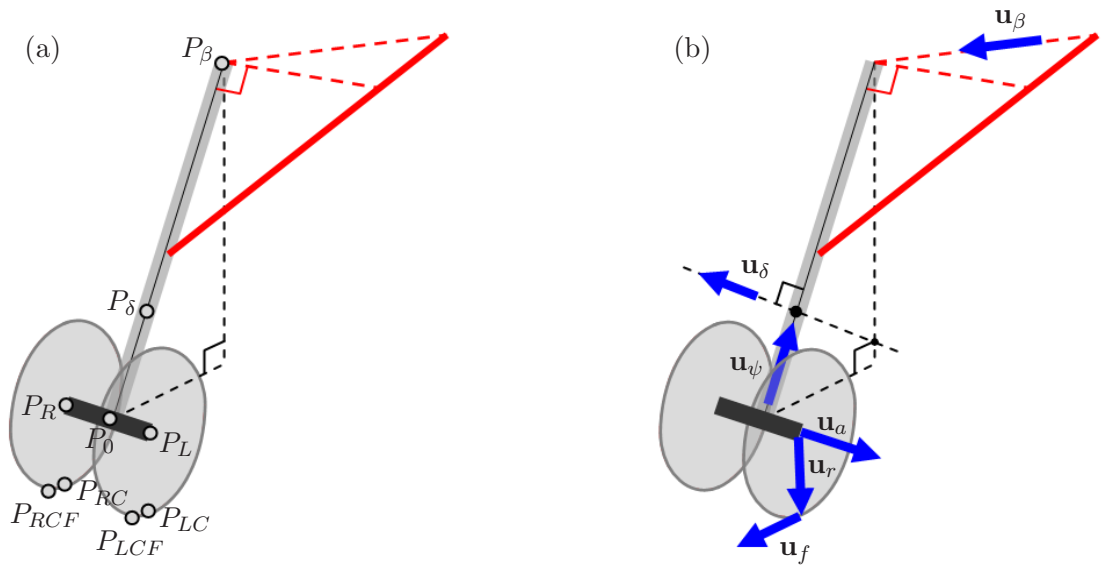

Figure 5: Points (a) and unit vectors (b) allowing calculation of the moments acting on the system. Note that for non-zero caster lengths ($e \neq 0$) point P_0 is not in line with P_L and P_R.

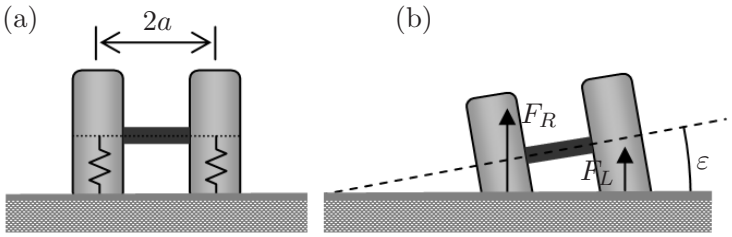

Figure 6: Dual-wheel configuration with separation distance $2a$ (a). Left (F_L) and right (F_R) reaction forces acting on the system (b) are calculated using a static force balance for an axle inclined at an angle ε to the ground plane.

frame as:

$$\mathbf{u}_{\psi 0} = \begin{pmatrix} -\sin\phi_0 \\ 0 \\ \cos\phi_0 \end{pmatrix}, \quad \mathbf{u}_\beta = \begin{pmatrix} -\cos\rho\sin\mu \\ -\cos\rho\cos\mu \\ -\sin\rho \end{pmatrix}, \qquad \mathbf{u}_{\delta 0} = \begin{pmatrix} \cos m\cos\phi_0 \\ -\sin m \\ \cos m\sin\phi_0 \end{pmatrix},$$

$$\mathbf{u}_\psi = R(\mathbf{u}_\beta, \beta)R(\mathbf{u}_{\delta 0}, \delta_0)\mathbf{u}_{\psi 0}\,, \qquad \mathbf{u}_\delta = R(\mathbf{u}_\beta, \beta)\mathbf{u}_{\delta 0}\,,$$

$$\mathbf{u}_\lambda = \frac{1}{|(\mathbf{u}_{a,X}\,, \mathbf{u}_{a,Y}\,, 0)|}(\mathbf{u}_{a,X}\,, \mathbf{u}_{a,Y}\,, 0)\,, \qquad \mathbf{u}_a = R(\mathbf{u}_\beta, \beta)R(\mathbf{u}_{\delta 0}, \delta)R(\mathbf{u}_{\psi 0}, \psi_s)\mathbf{e}_Y\,,$$

$$\mathbf{u}_f = \frac{1}{|(\mathbf{u}_{a,Y}\,, -\mathbf{u}_{a,X}\,, 0)|}(\mathbf{u}_{a,Y}\,, -\mathbf{u}_{a,X}\,, 0)\,, \qquad \mathbf{u}_r = R(\mathbf{u}_f, -\pi/2)\mathbf{u}_a\,.$$

Given these vectors, we are now able to define the moment terms acting on the MLG system, which may be

written as:

$$M_\psi = [\ (\mathbf{P}_{LC} - \mathbf{P}_0)\ \times \mathbf{F}_L + (\mathbf{P}_{RC} - \mathbf{P}_0) \times \mathbf{F}_R + (\mathbf{P}_C - \mathbf{P}_0) \times \mathbf{F}_\lambda - \mathbf{M}_\alpha\ ] \cdot \mathbf{u}_\psi\ \ , \tag{7}$$

$$M_\delta = [\ (\mathbf{P}_{LC} - \mathbf{P}_\delta)\ \times \mathbf{F}_L + (\mathbf{P}_{RC} - \mathbf{P}_\delta)\ \times \mathbf{F}_R + (\ \tfrac{1}{2}(\mathbf{P}_{LC} + \mathbf{P}_{RC}) - \mathbf{P}_\delta)\ \times \mathbf{F}_\lambda\ ] \cdot \mathbf{u}_\delta\ \ , \tag{8}$$

$$M^*_\beta = [\ (\mathbf{P}_{LC} - \mathbf{P}_\beta) \times \mathbf{F}_L + (\mathbf{P}_{RC} - \mathbf{P}_\beta) \times \mathbf{F}_R + (\ \tfrac{1}{2}(\mathbf{P}_{LC} + \mathbf{P}_{RC}) - \mathbf{P}_\beta) \times \mathbf{F}_\lambda\ ] \cdot \mathbf{u}_\beta\ \ ,$$

$$M_\beta = M^*_\beta - M_\psi(\mathbf{u}_\beta \cdot \mathbf{u}_\psi)\ \ . \tag{9}$$

Here M_β takes a more complex form due to the coupling between the modes ψ and β. The term $\mathbf{F}_\lambda = \mathbf{u}_\lambda F_{k\lambda}$ represents the combined side force produced by both tyres.

We split the vertical force F_z acting on the system into separate reaction forces F_L and F_R. This is achieved by considering a static force balance on the wheel assembly, for tyres of vertical stiffness k_t and an angle ε between the wheel axle and ground plane; see figure 6. This allows these reaction forces to be written as

$$\mathbf{F}_{L,R} = (1/2F_z \mp a\varepsilon k_t)\, \mathbf{e}_Z\ ,$$

where $\varepsilon = \sin^{-1}(\mathbf{u}_{a\,Z})$.

Finally, we consider the term $\mathbf{M}_\alpha$ in equation (7), which represents the restoring moment exerted by the tyres onto the landing gear. It is given by

$$\mathbf{M}_\alpha = \left(M_{k\alpha} + c_\lambda \dot{\psi} \mathbf{u}_{\psi\,Z} V^{-1}\right) \mathbf{e}_Z\ ,$$

and is a consequence of both the stiffness and damping properties associated with the warping of the tyre contact patch regions. Here c_λ denotes the rotational damping of the contact patch area, having a decreasing effect on the system dynamics as the forward velocity of the system increases, and $M_{k\alpha}$ represents the rotational stiffness and is given by equation (6). We assume that the effect of this restoring force is felt only by the torsional mode of the system, and so the term only appears in equation (7).

With the addition of these terms we may now represent the full dynamics of the MLG as given by equations (1)–(4) with the moment terms as defined in equations (7)–(9). To study the behaviour of these equations, we also require a representative set of parameter values for a main landing gear. We choose the values as listed in table 1, which are taken in part from [31] with a careful selection of the other parameters to ensure realistic and sufficiently distinct linear frequencies of 9.81 Hz, 16.05 Hz and 13.63 Hz for the ψ, δ and β modes, respectively. Although these parameter values do not come from a specific civil aircraft MLG, they serve to represent a generic landing gear system that may experience shimmy instability. In particular, they allow us to study the additional effects of a variable side-stay geometry on the shimmy dynamics. Note that the ranges of the continuation parameters V and F_z are deliberately chosen larger than their operational ranges in order to ensure that all features of the bifurcation diagrams are captured.

3 Analysis of the Perpendicular Case $\mu = 0^\circ$

We now turn our attention to the simplest side-stay orientation of the MLG, in which the line between the attachment points is horizontal and perpendicular to the direction of travel. We therefore set $\rho = 0^\circ$ throughout and consider first the case that $\mu = 0^\circ$; in turn this implies that both $p = 0$ and $m = 0$; see figure 3. Consequently, in this case the modes only couple through the tyre forces. Moreover, the in-plane mode δ corresponds to motion lateral to the direction of travel of the aircraft, while the out-of-plane mode β corresponds to motion in the longitudinal direction of the aircraft. Hence, based on the observations in [31, 32] for a NLG, one would expect δ to play a big role in the dynamics, with negligible coupling to β for this special case of $\mu = 0^\circ$. In the following sections we provide examples of the different types of shimmy oscillations of the MLG and then use a bifurcation analysis to determine the parameter regions in the (V, F_z)-plane of forward velocity and vertical force, in which this behaviour may be observed.

Symbol	MLG parameter	Value	Units
Geometric parameters			
ρ	attachment point inclination	0	deg
μ	horizontal attachment point orientation angle	0 – 90	deg
e	caster length	0.12	m
ϕ_0	static rake angle	0.05236	rad (3°)
a	half track width	0.25	m
L_δ	radius of in-plane deflection	0.75	m
L_β	gear length	2.5	m
Structural parameters			
I_ψ	torsional inertia	100	kg m^2
I_δ	in-plane inertia	600	kg m^2
I_β	out-of-plane inertia	750	kg m^2
c_ψ	torsional damping	300	N m s rad^{-1}
c_δ	in-plane damping	300	N m s rad^{-1}
c_β	out-of-plane damping	300	N m s rad^{-1}
k_ψ	torsional stiffness	3.8×10^5	N m rad^{-1}
k_δ	in-plane stiffness	6.1×10^6	N m rad^{-1}
k_β	out-of-plane stiffness	5.5×10^6	N m rad^{-1}
Tyre parameters			
r	tyre radius	0.362	m
h	contact patch length	0.1	m
L	relaxation length	0.3	m
k_t	vertical tyre stiffness	7×10^5	N m^{-1}
k_α	tyre self-aligning coefficient	1.0	m
k_λ	tyre restoring coefficient	0.002	rad^{-1}
c_λ	tyre damping coefficient	570	N m^2 rad^{-1}
α_m	maximum slip angle	0.1745	rad (10°)
Continuation parameters			
V	forward velocity	0 – 350	m s^{-1}
F_z	vertical force	0 – 10^6	N

Table 1: Parameters and their values as used in the analysis of the MLG.

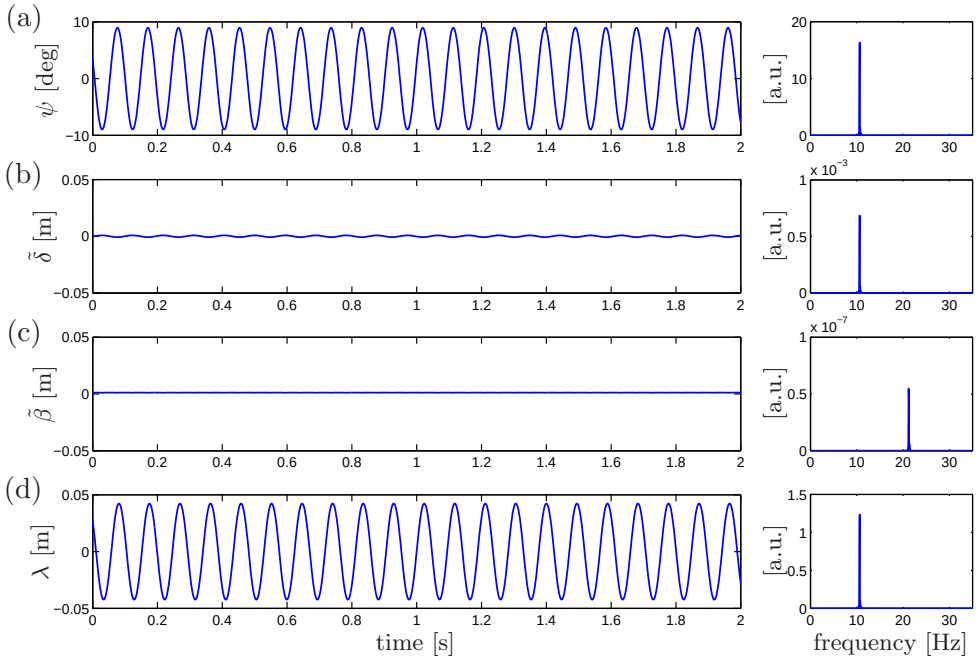

Figure 7: Torsional ψ-shimmy oscillations of the MLG with $\mu = 0$ for $V = 40$ m/s and $F_z = 10^5$ N. Shown are time series and the corresponding frequency spectra (in arbitrary units) of the torsional angle ψ, of the deflections $\tilde{\delta}$ and $\tilde{\beta}$, and of the tyre deflection λ.

3.1 Examples of Shimmy Oscillations

To illustrate the existence of shimmy oscillations we numerically integrate equations (1)–(4). Figures 7 and 8 give resulting time series for ψ, δ, β and λ, shown along with the corresponding frequency spectra. Throughout, the magnitude of the torsional mode ψ is given in degrees, while the modes δ and β are represented by the resulting deflections $\tilde{\delta}$ and $\tilde{\beta}$ at the bottom of the strut (at the point $\triangle\mathbf{P_0}$ in figure 5(a)); note that this definition is slightly different from that used in [31, 32], where the deflections are considered at ground level.

Figure 7 is for $V = 40$ m/s and $F_z = 10^5$ N. We see that for this case all three modes display oscillatory motion, but that the torsional mode ψ dominates the response with a relatively large amplitude of nearly 10° degrees. In comparison, the modes δ and β produce deflections $\tilde{\delta}$ and $\tilde{\beta}$ at the strut tip in the sub-millimetre range. Furthermore, we note that both the modes ψ and δ are locked into a frequency of ~ 10.6 Hz with the mode β oscillating at a frequency of twice this value. This characteristic frequency lies closest to the linear torsional frequency of 9.8 Hz, further emphasising the torsional dominance within this response. As a final clarification we note that the lateral deflection λ of the tyres shows periodic dynamics at the frequency and phase of the torsional mode. Therefore, based on these results we determine that for this choice of parameters the MLG displays torsional or ψ-shimmy with the system passively following the torsional mode ψ in-phase.

Figure 8 shows the MLG response for $V = 100$ m/s and $F_z = 4 \times 10^5$ N. Again we observe oscillatory behaviour of the system; however, the in-plane mode δ is now dominating the response. Moreover, this happens at a frequency of about 15.5 Hz, which now lies closest to the linear frequency of δ of 16.1 Hz. We also note that the lateral tyre deflection λ now oscillates with the frequency of the mode δ with a phase shift of $\pi/2$ rad. As before, this observation may be used to identify this type of shimmy as in-plane or δ-shimmy. Since the side-stay orientation angle μ is zero, the mode δ in the side-stay plane is perpendicular to the direction of travel of the aircraft. Therefore, δ-shimmy is also referred to as lateral shimmy of the MLG in this case, which is still justified when μ is sufficiently small.

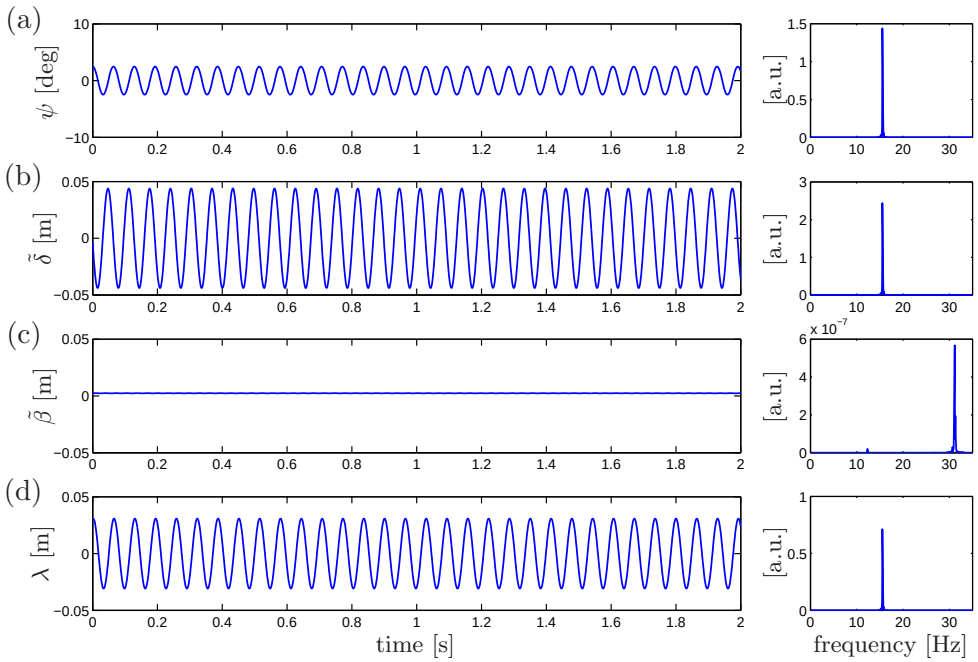

Figure 8: Lateral δ-shimmy oscillations of the MLG with $\mu = 0$ for $V = 100$ m/s and $F_z = 4 \times 10^5$ N. Shown are time series and the corresponding frequency spectra (in arbitrary units) of the torsional angle ψ, of the deflections $\tilde{\delta}$ and $\tilde{\beta}$, and of the tyre deflection λ.

Overall, we observe that, depending on the parameter range in question, the system may display different types of shimmy oscillations, each corresponding to a different characteristic frequency, with the MLG experiencing a different contribution from one of the three basic modes of oscillation. Another point to note is that we have not yet seen out-of-plane or β-shimmy oscillations, where the mode β is dominant in the MLG response. In the two cases of shimmy oscillations presented, the magnitude of the mode β remains very small, while it passively follows the modes ψ or δ through coupling via the tyre. Any larger perturbations to the mode β simply cause it to perform damped oscillations at its own frequency, thus returning to a small and passive amplitude response. For a MLG with a perpendicular side-stay with $\mu = 0^\circ$ the mode β lies in the direction of travel of the aircraft. Oscillations in β are, hence, also referred to as longitudinal shimmy of the MLG when μ is sufficiently small. In other words, we did not find longitudinal shimmy oscillations when $\mu = 0^\circ$, which can be attributed to the fact that the mode β is not sufficiently coupled with the other modes of the system to contribute to the shimmy dynamics. This finding agrees with the results in [31] for a NLG model represented by basic longitudinal, lateral and torsional modes. Therefore, in this section that considers the case $\mu = 0^\circ$, we restrict ourselves to showing only the torsional mode ψ and the (lateral) in-plane mode δ.

3.2 One-Parameter Continuation

We now identify the parameter regions in which the MLG system may experience shimmy oscillations. We choose as our bifurcation parameter the forward velocity of the system V, while fixing F_z at a specific value and setting the other parameters as given in table 1. This is a natural choice of bifurcation parameter as, in reality, the shimmy oscillations of landing gear systems are often only observed within a specific velocity range, suggesting an inherent sensitivity to variations in its value. One-parameter bifurcation diagrams are obtained with the continuation software AUTO [11]; to reflect our previous examples we choose values for the loading force F_z that match those already considered. Figure 9 (a1) and (a2) shows results for $F_z = 2 \times 10^5$ N,

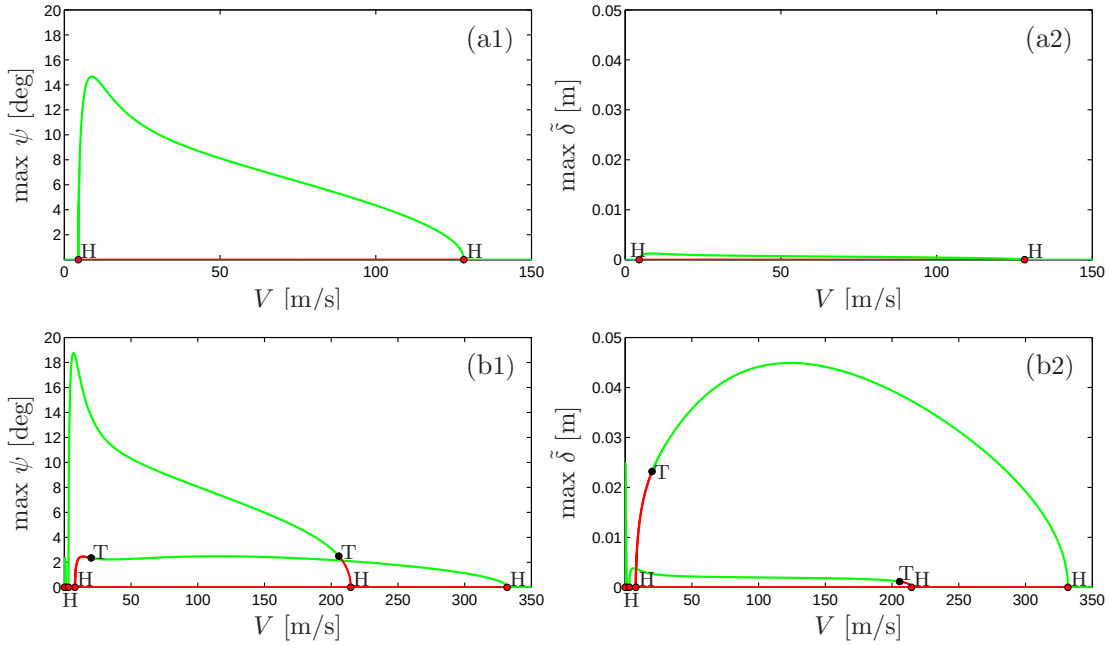

Figure 9: One-parameter bifurcation diagrams in V of the MLG with $\mu = 0$ for a vertical force of $F_z = 2 \times 10^5$ N in panels (a) and of $F_z = 4 \times 10^5$ N in panels (b); shown are the maxima of the torsional angle ψ (left column) and of the in-plane deflection $\tilde{\delta}$ (right column). Stable solutions are green and unstable solutions are red; Hopf bifurcation points (H) are shown as red dots, and torus bifurcation points (T) as black dots.

showing oscillatory solutions in terms of the amplitudes of the torsional mode ψ and of the deflection $\tilde{\delta}$ of the in-plane mode δ, respectively. Non-oscillatory straight-line rolling of the MLG is given by the zero-amplitude solution, which exists over the entire velocity range considered. However, as the forward velocity is increased, the stability of this straight-rolling solution changes: stability is lost and then regained when two supercritical Hopf bifurcation points are passed. These two bifurcation points are connected by a branch of stable periodic orbits, indicating the appearance of shimmy oscillations in the dynamics. Within the velocity range bounded by the two Hopf points the dynamics of the MLG will move away from the straight-rolling solution, and one observes the onset of shimmy oscillations, with amplitudes of ψ and $\tilde{\delta}$ as shown in the figure (the amplitude of $\tilde{\beta}$ remains extremely small throughout and is not shown). We note from figure 9(a) that the (torsional) ψ-component of this periodic solution is significantly greater than the (lateral) $\tilde{\delta}$-component, and indeed the entire branch of periodic orbits represents torsional ψ-shimmy; compare with figure 7.

Figure 9 (b1) and (b2) show one-parameter bifurcation diagrams for a loading force of $F_z = 4 \times 10^5$ N. Apart from the previous branch of periodic orbits representing torsional shimmy, we now note the existence of a second branch of periodic solutions connecting a second pair of Hopf bifurcation points. The amplitudes of ψ and $\tilde{\delta}$ along this branch show that the oscillations have a strong δ-component, and we conclude that this branch represents (lateral) in-plane δ-shimmy of the MLG; see figure 8. Regarding the stability of the system, from figure 9 (b1) and (b2) we note that the straight-rolling solution is again unstable over the entire velocity range spanned by the periodic orbits. For lower values of the forward velocity we see that this results in torsional shimmy oscillations, whereas for higher velocity values the MLG experiences lateral shimmy. We also note that there exists a velocity range (here $V \in (19.5, 205.7)$), bounded by torus bifurcation points, over which both periodic solutions are stable. Depending on the initial condition of the system and the presence of external perturbations, one may see either torsional or lateral shimmy in the MLG response for $\mu = 0^\circ$.

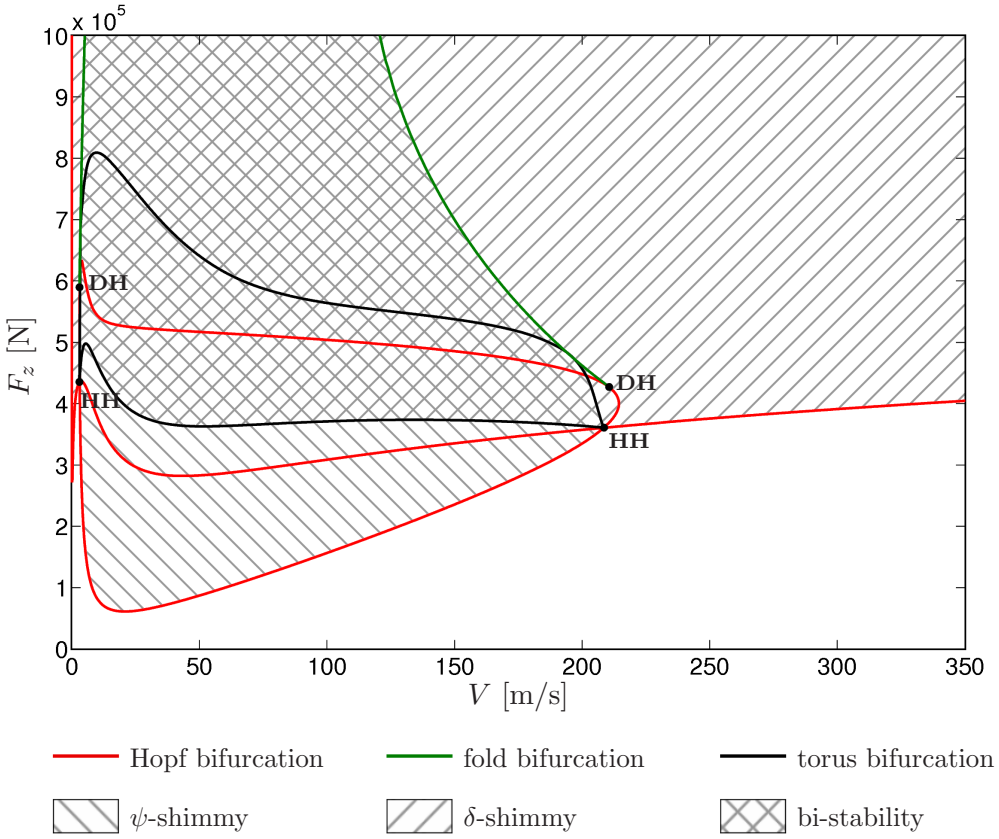

Figure 10: Bifurcation diagram in the (V, F_z)-plane of the MLG for $\mu = 0$ with regions of torsional ψ-shimmy and with (lateral) in-plane δ-shimmy oscillations. The points labelled HH and DH are codimension-two double Hopf and degenerate Hopf points, respectively.

3.3 Two-Parameter Bifurcation Diagram

Motivated by the results of the previous section we now explore the system dynamics for a continuous range of the vertical force F_z rather than for the two discrete values previously considered. We therefore continue the codimension-one bifurcations identified in the previous section in the two-parameter (V, F_z)-plane of forward velocity V and loading force F_z. Figure 10 shows the resulting bifurcation diagram. It consists of a closed curve of super-critical Hopf bifurcations that intersects a second Hopf bifurcation curve (again super-critical) at a pair of Hopf-Hopf points (HH). These codimension-two points are important in determining the local structure of the dynamics and, as expected from general bifurcation theory, they lead to the emergence of two curves of torus (or Neimark-Sacker) bifurcations, the lower of which forms part of the stability boundary where the in-plane mode δ becomes undamped. We also see curves of saddle-node (or fold) bifurcations of periodic orbits — emanating from degenerate Hopf points (DH) of the closed Hopf bifurcation curve — that act as further stability boundaries of the system. In particular, they form the boundaries of torsional shimmy oscillations for higher values of F_z and are, in fact, parts of a single fold curve connecting the two degenerate Hopf points.

Overall, the bifurcation diagram in the (V, F_z)-plane provides a global view of the dynamics of the MLG. The non-shaded region at the bottom of figure 10 shows the desirable parameter region in which the non-oscillatory straight-rolling solution is stable. As the loading force is increased this solution loses stability; this results in shimmy oscillations, which may be torsional or in-plane (lateral) in nature (depicted by left- and right-slanted shading, respectively). In agreement with what we saw in the last section, only torsional shimmy may be observed for low values of F_z. Lateral shimmy, on the other hand, may be found for larger loading

forces, and it may coexist with torsional shimmy in a large region of bistability. A final point to note is that the bifurcation diagram in figure 10 also serves to validate our model against existing results. Specifically, we see that our MLG model for $\mu = 0^\circ$ has the same qualitative features as were found in [31] for a study of a NLG (with similar parameters and modelling assumptions). Indeed, for $\mu = 0^\circ$ our model reproduces many of the dynamical characteristics found in NLG shimmy, including the presence of bi-stability.

4 Effect of Side-Stay Orientation Angle μ

The bifurcation diagram in the (V, F_z)-plane in figure 10, and the associated regions of different types of shimmy oscillations, depend on the values of other parameters. We focus now on the effect of changing the side-stay angle μ over the range $\mu \in [0^\circ, 90^\circ]$. This parameter is of specific interest, because μ varies greatly from aircraft to aircraft and, in general, cannot be assumed to be zero or even small. Note that for non-zero values of μ the orientation of the out-of-plane mode β differs from the orientation of the tyres. Via the tyre dynamics this leads in turn to an increasing geometric coupling between all three basic modes (which is not present for the special case $\mu = 0^\circ$). Moreover, for $\mu \neq 0^\circ$ the modes δ and β are no longer perfectly aligned with the lateral and longitudinal directions with respect to the direction of travel. Rather, δ and β both represent lateral as well as longitudinal components for intermediate values of μ, until for $\mu = 90^\circ$ their roles are exchanged with δ being a purely longitudinal mode and β being a purely lateral mode with respect to the direction of travel. In order to study the effect of this geometric coupling between the three basic modes ψ, δ and β, we consider how the bifurcation diagram in the (V, F_z)-plane changes with the side-stay angle μ; all other parameters remain fixed as specified in table 1.

4.1 Hopf Frequency Diagrams

The curves of Hopf bifurcations play an important role in the dynamics of the MLG system: they generate different types of shimmy oscillations and are largely responsible for the overall structure of the bifurcation diagram in the (V, F_z)-plane. For this reason we first consider how the Hopf bifurcation curves alone change when the side-stay angle μ is increased from $\mu = 0$. Since types of shimmy oscillations are characterised by having a frequency close to the linear frequency of the corresponding mode, it is of interest to consider also the frequencies of the periodic orbits that bifurcate from the Hopf bifurcations. We therefore construct two-parameter diagrams in the (V, F_z)-plane of Hopf bifurcation curves, where colour represents the frequency of the bifurcating periodic solutions as determined from the purely imaginary eigenvalues.

Figure 11 shows this type of Hopf frequency diagram for several representative values of μ ranging from 0° to 90°. The corresponding colour map shows the linear frequencies of the modes ψ, δ and β as blue, red and light green, respectively. Overall, one notices considerable changes in the Hopf bifurcation curves when μ is increased from $\mu = 0^\circ$ to $\mu = 90^\circ$. These two extreme values of μ represent the simplest cases of the MLG system with effectively only two contributions to shimmy oscillation frequencies present in the dynamics: that of the modes ψ and δ for $\mu = 0^\circ$, and that of the modes ψ and β for $\mu = 90^\circ$. Recall that δ is defined as motion in the plane of the side-stay, while β models motion perpendicular to the side-stay plane. Hence, β is aligned with the direction of aircraft motion only for small values of the side-stay angle μ. For μ near 90°, on the other hand, the mode δ is aligned with the longitudinal direction; hence, it is geometrically uncoupled from the other two modes, and β now corresponds to lateral motion with respect to the direction of aircraft motion. In addition, as with β when μ is small, for μ near 90° the mode δ is geometrically uncoupled from the other two modes. This explains the degree of similarity of figure 11(a) and (h) for $\mu = 0^\circ$ and $\mu = 90^\circ$, respectively, with the roles of δ and β exchanged. For intermediate μ values, however, the bifurcation diagram is considerably more complex due to the coupling of all three basic modes.

The transition between $\mu = 0^\circ$ and $\mu = 90^\circ$ in figure 11 is marked by several qualitative changes of the Hopf bifurcation curves. Moreover, the colour map shows how this is associated with changes to the frequency of the bifurcating oscillations. Figure 11(a) shows the two Hopf bifurcation curves for $\mu = 0$; compare with figure 10. The red curve is clearly associated with oscillations of the mode δ, while the other gives rise to stable torsional shimmy oscillations in ψ along the (blue) section below the other (red) Hopf bifurcation curve. The

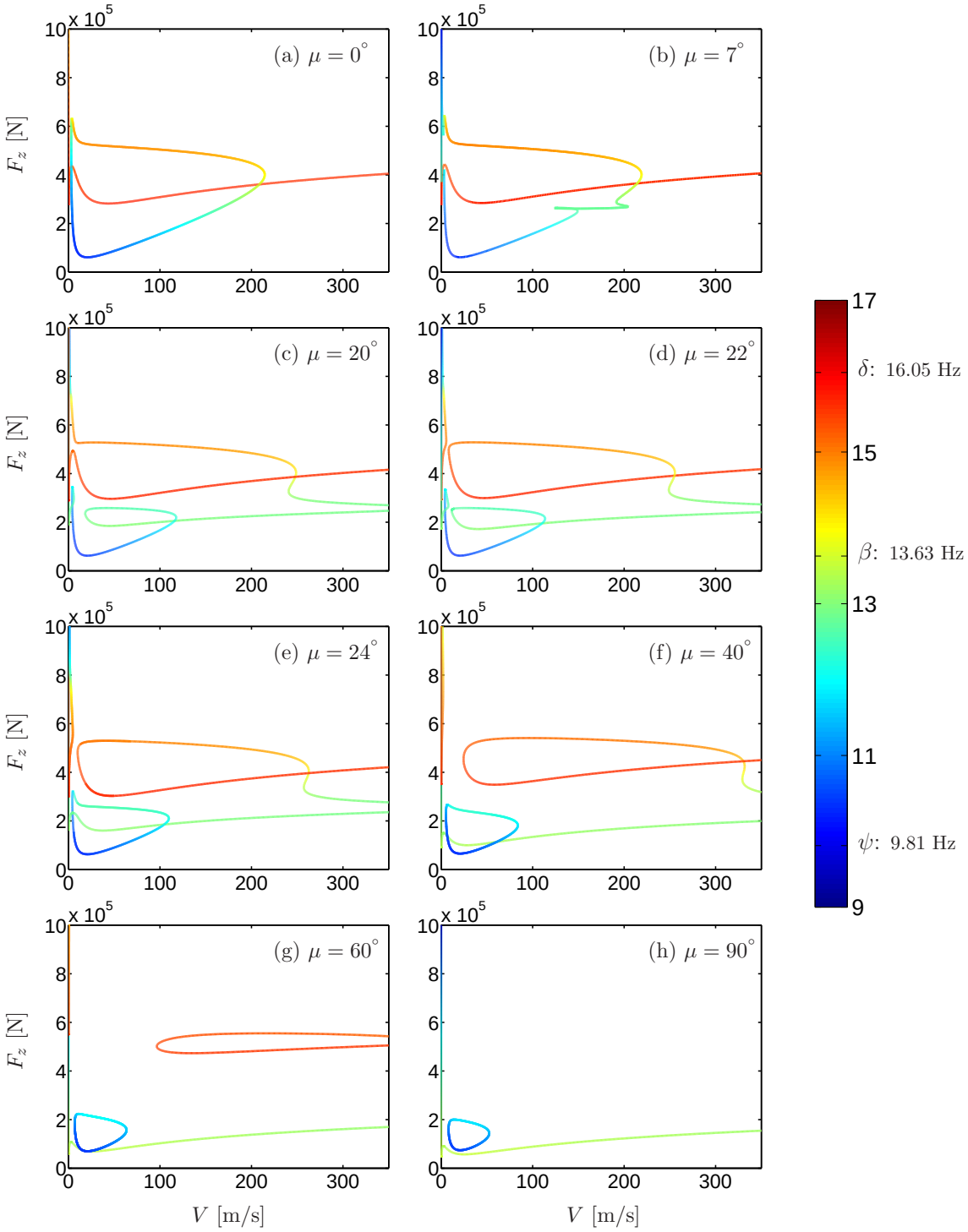

Figure 11: The Hopf bifurcation curves in the (V, F_z)-plane of the MLG for multiple side-stay orientation angles in the range $\mu \in [0^\circ, 90^\circ]$; colour represents the frequency of the bifurcating periodic solution as given by the colour map.

first qualitative change occurs for a side-stay angle of $\mu \approx 7^\circ$, when a loop appears in one of the Hopf curves; see figure 11(b). Notice further, the associated (green) section of this Hopf bifurcation curves, giving rise to oscillations with a frequency near the linear frequency of the out-of-plane mode β. This Hopf bifurcation curve

consequently intersects itself at a double Hopf point (at $V \approx 145$ m/s), which has a profound influence on the structure of the two-parameter bifurcation diagram as we will see in the next section. This loop grows to considerable size when μ is increased to $\mu = 20^\circ$. Moreover, there emerges a nearly horizontal (green) section of this Hopf bifurcation curve associated with oscillations in β; see figure 11(c). In effect, the upper boundary of the stability region of the straight-rolling solution is now formed by one and the same self-intersecting Hopf bifurcation curve in the region of interest. Between $\mu = 20^\circ$ and $\mu = 22^\circ$ there is a change in the connectivity of the two Hopf bifurcation curves at $(V, F_z) \approx (7, 5.1 \times 10^5)$, and another such change occurs between $\mu = 22^\circ$ and $\mu = 24^\circ$ at $(V, F_z) \approx (9, 2.6 \times 10^5)$; compare panels (c)–(e) of figure 11. These changes are due to the fact that the slice $\mu = const$ moves through a saddle point of the surface of Hopf bifurcations in (V, F_z, μ)-space, and we refer to this phenomenon as a saddle transition of the Hopf bifurcation curves; for other examples of this phenomenon see [33] regarding NLG and [12, 14, 16] more generally. As a result of these transitions we find that for $\mu = 24^\circ$ and above a closed (blue) curve of Hopf bifurcations is intersected by a (green) Hopf bifurcation curve — a structure that is remarkably like what we found for $\mu = 0^\circ$ but with the roles of δ and β exchanged. Additionally, there is a (red) section of the Hopf bifurcation curve associated with oscillations in δ, but at considerably higher values of F_z; see figure 11(e). This (red) section moves towards higher values of V with increasing μ. At the same time the (green) curve of Hopf bifurcations that generates oscillations in β moves towards lower values of F_z; see figure 11(f) and (g). Finally, for $\mu = 90^\circ$ the section of Hopf bifurcations associated with oscillations in δ has left the region of interest in the (V, F_z)-plane shown in the figure. Moreover, the two remaining curves of Hopf bifurcations no longer intersect each other; see figure 11(h). As a result, the stability boundary of straight rolling is formed by the (green) Hopf bifurcation curve alone, meaning that as the vertical load is increased one would expect to first see β-shimmy oscillations. Since $\mu = 90^\circ$, these oscillations correspond to lateral shimmy.

4.2 Two-Parameter Bifurcation Diagrams

Overall, the changes in the Hopf frequency diagram in figure 11 indicate the sensitivity of the system to variations in side-stay orientation angle μ, as well as the increasingly prominent role of the out-of-plane mode β as μ is increased. We now present in figure 12 the associated two-parameter bifurcation diagrams for each of the eight chosen values of μ over the transition from $\mu = 0^\circ$ to $\mu = 90^\circ$. Each bifurcation diagram in figure 12 shows curves of Hopf bifurcations, saddle-node bifurcations of periodic orbits, and torus bifurcations. The shaded regions are the stability regions of torsional ψ-shimmy (left slanted), of in-plane δ-shimmy (right slanted), and of out-of-plane β-shimmy (dotted). Comparison of the respective panels of figures 12 and 11 shows that the Hopf bifurcation curves alone only hint at the stability regions of the different types of shimmy oscillations. The aim of figure 12 is to illustrate the overall complexity of regions of stable oscillations in the transition from $\mu = 0^\circ$ to $\mu = 90^\circ$; on the other hand, it does not show the details of all transitions of the different bifurcation curves. The overall structure of the bifurcation diagrams in figure 12 is organised throughout by the codimension-two double Hopf and degenerate Hopf points as well as the emerging curves of saddle-node and torus bifurcations of periodic orbits.

Panel (a) of figure 12 for $\mu = 0^\circ$ is the starting point; it is repeated from figure 10. Increasing μ to 7° we already find a (dotted) region of β-shimmy oscillations (where the out-of-plane mode β dominates) in the vicinity of the newly created double Hopf point at $V \approx 145$m/s; the region is bounded below by the nearly horizontal section of the lower Hopf bifurcation curve, and to the sides by torus and saddle-node bifurcation curves that are associated with double Hopf and degenerate Hopf points; see figure 12(b). Note that for $\mu = 7^\circ$ there is no clear upper boundary of the region of β-shimmy. Rather, we see a gradual transition in frequency and mode shape from β-shimmy to torsional ψ-shimmy as the loading force F_z is increased. Since μ is still very small, β-shimmy is effectively longitudinal shimmy. In other words, even a small geometric coupling between the three basic modes may result in the observation of considerable longitudinal oscillations of the MLG.

When μ is increased to $\mu = 20^\circ$, the region of β-shimmy (which is still largely in the longitudinal direction) increases, both towards larger values of V and towards larger values of F_z; see figure 12(c). In fact, when F_z is increased for a velocity V above 120 m/s, out-of-plane β-shimmy, rather than in-plane δ-shimmy is typically observed. We also note a change in the local connectivity of the torus bifurcation curves due to a saddle transition, that is, a transition through a saddle point in the surface of torus bifurcations in (V, F_z, μ)-space;

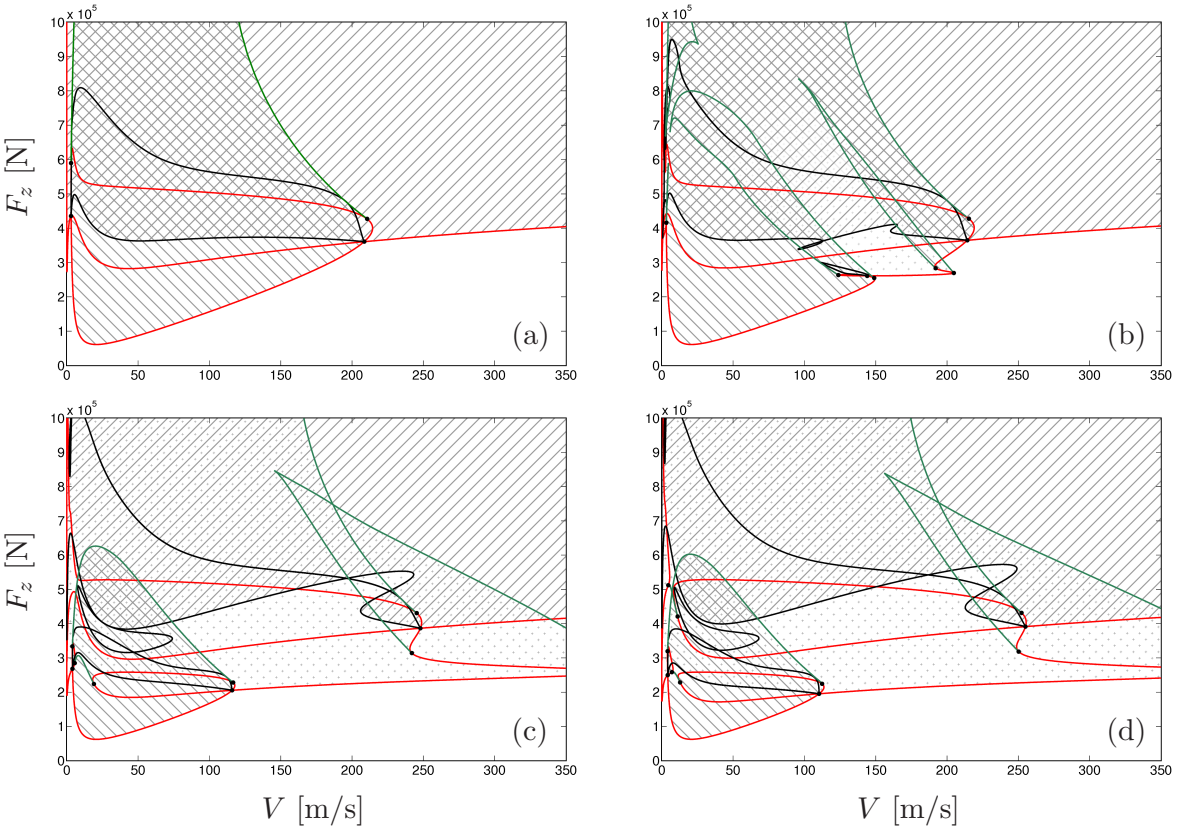

Figure 12: Bifurcation diagram of the MLG in the (V, F_z)-plane for $\mu = 0^\circ$ (a), for $\mu = 7^\circ$ (b), for $\mu = 20^\circ$ (c), for $\mu = 22^\circ$ (d). Shown are curves of Hopf bifurcations (red) of saddle-node bifurcations (green) and of torus bifurcations (black). In the white region the straight-rolling solution is stable; left-slanted shading denotes stable torsional ψ-shimmy oscillations, right-slanted shading denotes stable in-plane δ-shimmy oscillations, and dotted shading denotes stable out-of-plane β-shimmy oscillations. Panel (a) is repeated from figure 10.

see [33] for another example of such a transition. The bifurcation diagrams for $\mu = 22^\circ$ and $\mu = 24^\circ$ are very similar, differing only in the connectivity of the Hopf bifurcation curves; see figure 12(d) and (e). Here we see the presence of several regions of multiple stability; in particular, for $\mu = 24^\circ$ we find a region of tri-stability in which solutions of ψ-shimmy, δ-shimmy and β-shimmy co-exist in the dynamics. A further point of interest in the bifurcation diagrams in figure 12 is the formation of a local structure of bifurcation curves in the parameter range $V \in (0, 150)$, $F_z \in (0, 4.5 \times 10^5)$ that is very similar to the one found for $\mu = 0^\circ$. The structure is characterised by the interaction of two Hopf bifurcation curves (one of which is an isola) at two double Hopf bifurcation points with associated torus and saddle-node curves that bound regions of different types of shimmy oscillations; compare panels (e) and (a) of figure 12. The difference is that for $\mu = 0^\circ$ this structure involves the modes ψ and δ, while for $\mu = 24^\circ$ it involves the modes ψ and β. This is a clear indication of the exchange of the roles of δ and β for the dynamics of the MLG. The conclusion is that, even for such relatively small side-stay angles μ the out-of-plane mode plays a prominent role alongside the in-plane mode in the shaping the dynamics of the MLG system.

When μ is increased further to $\mu = 40^\circ$ and then $\mu = 60^\circ$, the isola of Hopf bifurcations associated with torsional oscillations shrinks and the intersecting Hopf bifurcation curve leading to β-oscillations moves down towards smaller values of F_z; see figure 12(f) and (g). At the same time, the remaining bifurcation curves move further up in F_z. Finally, the two lower Hopf bifurcation curves do not intersect any longer (following the transition through a codimension-three degenerate double Hopf bifurcation point) and all other bifurcation

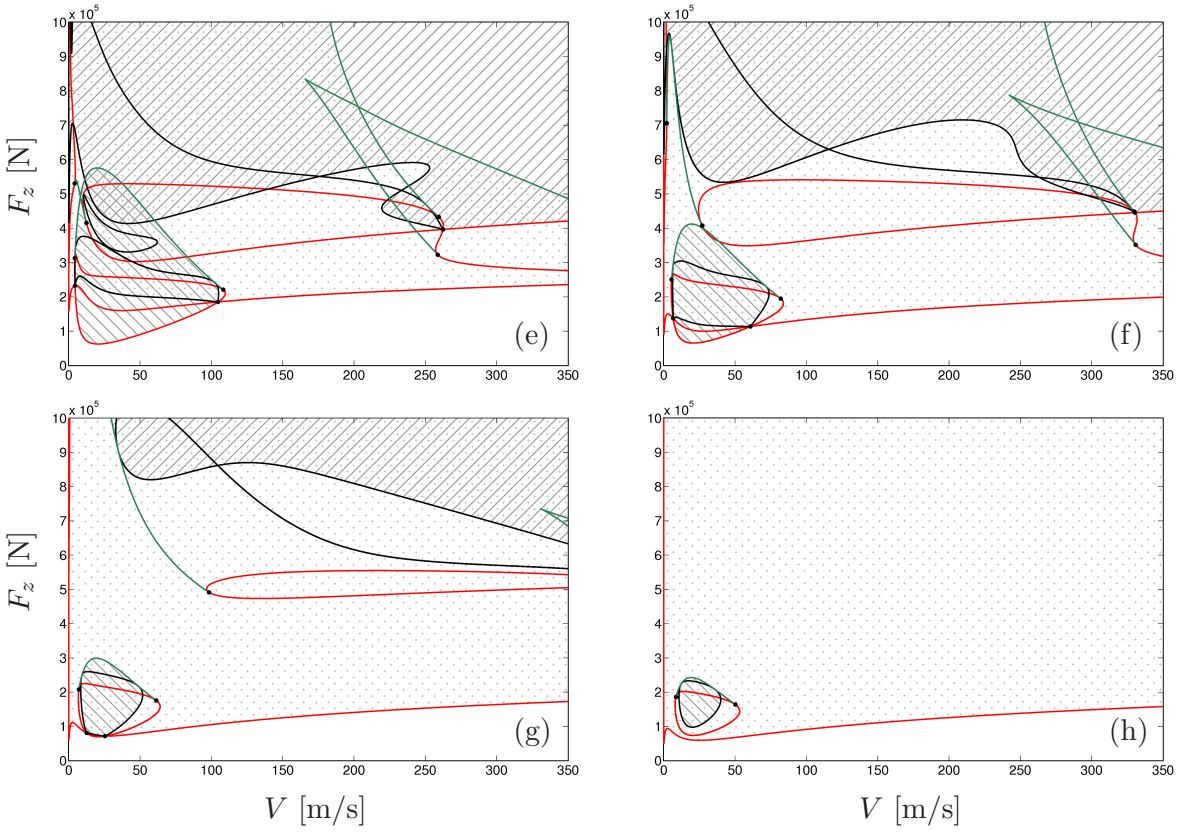

Figure 12: **Continued.** Bifurcation diagram of the MLG in the (V, F_z)-plane for $\mu = 24^\circ$ (e), for $\mu = 40^\circ$ (f), for $\mu = 60^\circ$ (g), and for $\mu = 90^\circ$ (h).

curves leave the region of interest of the (V, F_z)-plane. The result is the bifurcation diagram shown in figure 12(h) for $\mu = 90^\circ$. Apart from a small region of torsional ψ-shimmy one only finds stable β-shimmy once the straight-rolling solution becomes unstable. It is an important observation that for $\mu = 90^\circ$ the MLG has a geometry much like a NLG; indeed, the observation that the (lateral) out-of-plane mode β is dominant in this case, with no evidence of longitudinal dynamics, agrees well with the results in [31, 32] for a NLG.

We remark that the fixed region in the (V, F_z)-plane shown in figures 11 and 12 was deliberately chosen to be quite large, so that the qualitative changes of the bifurcation diagram show. A more realistic range of the velocity would be $V \in [0, 80]$ m/s. Notice, however, that qualitative changes of the bifurcation diagram outside of the MLG operating region do lead to changes of the observed shimmy phenomena over realistic parameter ranges; for example, we first see the out-of-plane mode appearing for $\mu = 7^\circ$ with the creation the new double Hopf point at $V \approx 145$m/s. Therefore it proves necessary in practice to consider an extended parameter range when exploring the full dynamics of the MLG system. As a final point we note that, as μ increases, the non-shaded region representing stable straight-rolling motion of the MLG shrinks. Overall this implies that, for this particular choice of parameters, the system is more likely to experience shimmy as $\mu \to 90^\circ$.

4.3 Tri-stable Behaviour

We observe in figure 12 large regions of multiple stability for intermediate values of μ. We remark that such behaviour is particularly undesirable from a design viewpoint, as sufficient perturbations to the system even near such a region may result in the observation of one of several types of shimmy. This makes it considerably more difficult to design a damper to safeguard against shimmy oscillations as one cannot be sure of the frequency

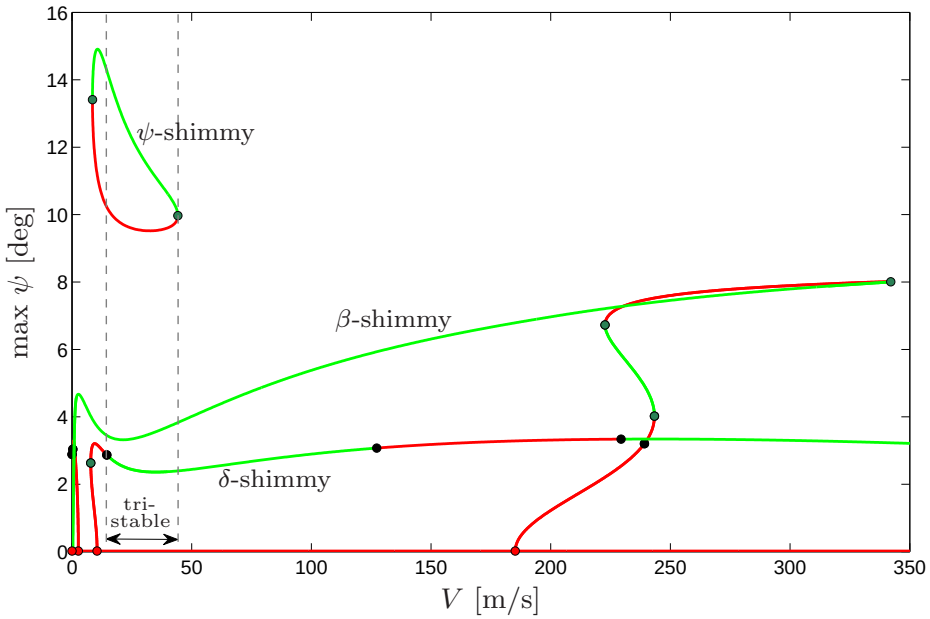

Figure 13: One-parameter bifurcation diagram in V of the MLG with $\mu = 24^{\circ}$ and for a vertical force value of $F_z = 5 \times 10^5$N, showing the maximum of the torsion angle ψ. Stable solutions are green and unstable solutions are red; The different branches of periodic solutions are labelled according to the type of shimmy oscillations they represent. Stable solutions are green and unstable solutions are red; also shown are points of Hopf bifurcation (red dots), saddle-node bifurcation (green dots), and torus bifurcation (black dots).

range to expect when the desired straight-rolling solution of the MLG becomes unstable.

To illustrate this point we now focus our attention on the most extreme case: the tri-stable region near $(V, F_z) \approx (30, 5 \times 10^5)$ for $\mu = 24^{\circ}$ in figure 12(e). We begin by considering the horizontal slice for $F_z = 5 \times 10^5$ through the region of interest. Figure 9 shows the one-parameter bifurcation diagram corresponding to this choice of loading force; shown are the bifurcating periodic solutions in terms of the amplitude of the torsional mode ψ. We observe the existence of three clearly distinguished periodic solutions in figure 9. They are labelled according to the type of shimmy oscillation they represent; torsional shimmy oscillations naturally have the highest magnitude of ψ. There are several regions of bi-stability and, importantly, all three types of shimmy oscillation coexists and are stable in the velocity range $V \in (14.6, 44.2)$; this range is bounded on the left by a torus bifurcation of in-plane δ-shimmy and on the right by a saddle-node bifurcation of the periodic orbit representing torsional ψ-shimmy. Notice that the ψ-shimmy oscillations occur along a closed loop, which is bounded by two saddle-node bifurcations and not connected to the straight-rolling solution. It may, hence, be missed in a one-parameter continuation that starts from the straight-rolling solution; however, is easily picked up from knowledge of the two-parameter bifurcation diagram in figure 12(e).

In the region of tri-stability the MLG may experience all three types of shimmy oscillation. The type that is observe in the dynamics of the landing gear depends on the initial condition, as well as on the nature of any possible external perturbations. By performing a numerical integration of the system for a choice of parameters within this region we may verify the co-existence of these three types of shimmy oscillations in the dynamics of the MLG and the possibility of switching between them by suitable perturbations. Figure 14 shows the results of a 60 second simulation run for $V = 30$ m/s and $F_z = 5 \times 10^5$ N. As in figures 7 and 8, the response of the system is shown as time series of ψ, $\tilde{\delta}$, $\tilde{\beta}$ and λ. The key feature of this simulation run is that we apply two perturbations as follows. At $t = 20$ s an impulse of 10 kNms is applied to the in-plane mode δ, and at $t = 40$ s an impulse of 4 kNms is applied to the out-of-plane mode β. In each case the perturbing force is applied

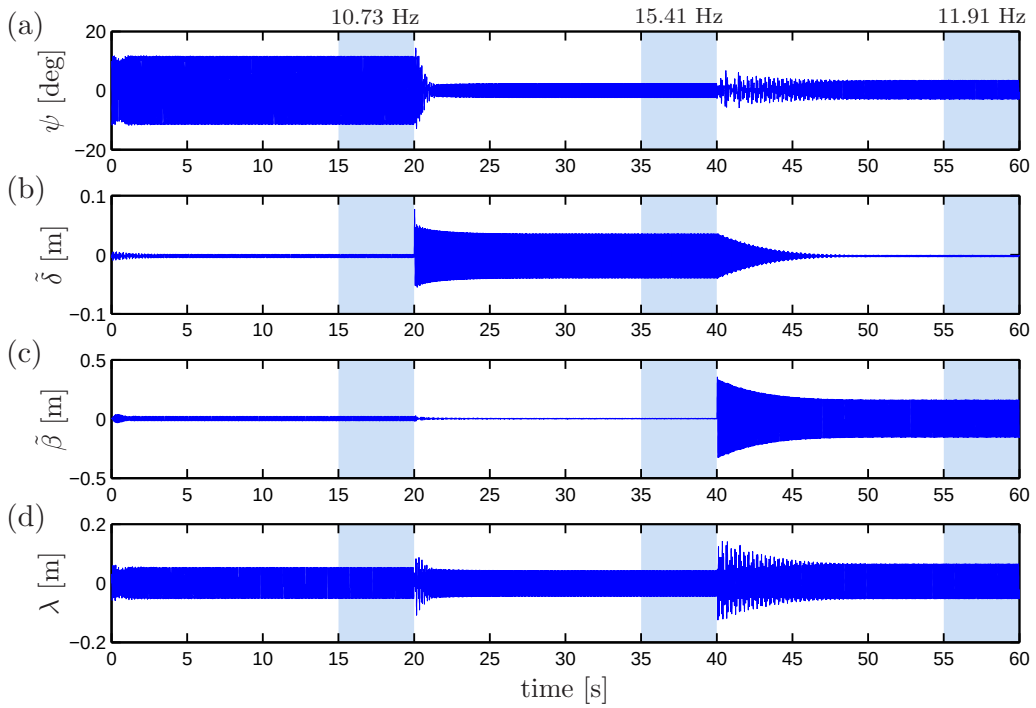

Figure 14: Simulation run within the tri-stable region for parameter values $(V, F_z) = (30, 5\times10^5)$. Perturbations are applied to the system at $t = 20$s to the in-plane mode δ and $t = 40$s to the out-of-plane mode β; as a result, the system moves between periodic solutions. The dominant frequency of the oscillation in the (shaded) five-second time windows is provided.

over 0.05 s. These two perturbations are sufficient to drive the system from one periodic solution to another, thus changing the type of shimmy oscillation experienced by the MLG. In particular, we see that the system moves from ψ-shimmy to δ-shimmy following the first perturbation, and then from δ-shimmy to β-shimmy as a consequence of the second perturbation. To emphasise the change in behaviour we also determine the dominant frequency of the oscillation over the five-second time window prior to each perturbation.

Figure 14 clearly shows that it is possible to switch between the different types of shimmy oscillations by an external perturbation of the MLG. We remark that such perturbations are not unrealistic from a physical viewpoint and may arise from a multitude of sources, including heavy braking of the aircraft, contact of the landing gear with a physical object, or traversal over an uneven runway surface. MLG systems may also experience large initial perturbations under heavy or non-symmetric landing conditions. These kinds of perturbations are largely unpredictable and, therefore, within regions of multiple stability a degree of uncertainty is introduced into the observable behaviour of the MLG.

5 Discussions and Future Work

We have presented a mathematical model of a dual-wheel MLG system and studied it by means of bifurcation analysis. Specifically, we constructed the bifurcation diagram in the (V, F_z)-plane of aircraft velocity and loading force on the gear, both of which are key operational parameters. This two-parameter bifurcation diagram provides a wealth of information on the observable dynamics of the MLG, telling us not only in which regions the MLG will oscillate but also which type of shimmy these oscillations represent. From a practical point of view, during take-off or landing the loading force F_z is a function of the velocity V: a take-off run corresponds to a path in the (V, F_z)-plane that starts from a given value of F_z (determined by the loading of the aircraft) at

$V = 0$ and ends at $F_z = 0$ at the take-off speed; similarly, a landing corresponds to a path that starts at $F_z = 0$ at the landing speed and ends at the taxi-speed with a given value of F_z (again determined by the loading of the aircraft). The bifurcation diagram in the (V, F_z)-plane can, hence, be used to evaluate the shimmy behaviour of the aircraft for take-off runs and landings under different conditions (loading of the aircraft and/or thrust settings), by considering how the respective curve (which can be measured in practice) intersects the bifurcation diagram.

Moreover, we showed that the influence of other parameters of interest can be studied by considering how the bifurcation diagram in the (V, F_z)-plane changes. In particular, we explored the effect of changing the orientation of the side-stay as given by the angle μ. From a practical point of view, this constitutes a design study as the parameter μ is determined at the early stages of the MLG design and cannot be changed during operations. We observed considerable sensitivity of the bifurcation diagram on μ when it was changed from $\mu = 0^\circ$ (side-stay perpendicular to direction of travel) to $\mu = 90^\circ$ (side-stay in line with direction of travel). Most aircraft feature side-stays with μ in the range of 20° to 40°, and we found quite a complex bifurcation diagram in this region of side-stay angles. In particular, three different types of shimmy oscillations can be observed in this range of μ, which are characterised by the dominance of the torsional, in-plane and out-of-plane modes. Moreover, we found considerable regions of multi-stability, including the coexistence of all three types of shimmy over a large range of realistic velocities. This is of interest from the design point of view, because the different shimmy oscillations are associated with different frequency ranges, which needs to be taken into account, for example, in the design of shimmy dampers.

The study presented here was for a typical landing gear, with parameters adapted from the literature, and its goal was to demonstrate what type of results can be obtained. Clearly, there are many directions for further research. First of all, some of the parameters that remained fixed here may also differ considerably from MLG to MLG. For example, the horizontal inclination ρ of the side-stay attachment relative to the attachment point of the main strut also influences the geometric coupling between the modes; what is its effect on the dynamics of the MLG? A second direction would be to consider MLG parameters that are more representative for a specific aircraft with a view of optimizing operations. For this purpose a study of the dynamics of the MLG in dependence on additional operational parameters, such as runway conditions or tyre pressure, would be suitable. Finally, we mention that there are a number of physical effects that are currently not included in the MLG model presented here, such as the dynamics of the shock absorber or freeplay in bearings. Given the versatility of the modelling approach employed here, it would be relatively straight forward to incorporate such effects into the MLG formulation, while still ensuring that it remains amenable to bifurcation analysis.

Acknowledgements

The authors thank Phanikrishna Thota for helpful discussions and Etienne Coetzee for sharing his insights, especially concerning the selection of suitable values for the parameters of the model. The research of C.H. was supported by a Knowledge Transfer Network (KTN) Mathematics CASE Award from the Engineering and Physical Sciences Research Council (EPSRC) in collaboration with Airbus in the UK.

References

[1] J. Baumann. A nonlinear model for landing gear shimmy with applications to the McDonnell Douglas F/A-18A. *AGARD-R-800*, 1995.

[2] J. Baumann, C. Barker, and L Koval. A nonlinear model for landing gear shimmy. In *Proceedings of the ASME Winter Annual meeting*, Atlanta, GA, December 1-6 1991.

[3] R. Bedford and M.L. Lowenberg. Bifurcation analysis of rotorcraft dynamics with an underslung load. *AIAA Atmospheric Flight Mechanics Conference*, AIAA-2004-4947, 2004.

[4] V. Bespalov, V. Metrikin, and M. Peisel. On the dynamic stiffness of a landing gear nose strut hydraulic damper system. *Izvestiya VUZ. Aviatsionnaya Tekhnika*, 32(3):3–6, 1989.

[5] G. Broulhiet. The suspension of the automobile steering mechanism: shimmy and tramp (in French). *Bull Soc. Ing. civ. Fr.*, 78:540–554, 1925.

[6] G. Charles, M. Lowenberg, D. Stoten, X. Wang, X., and M. di Bernardo. Aircraft flight dynamics analysis and controller design using bifurcation tailoring. *AIAA Guidance Navigation and Control Conference*, AIAA-2002-4751, 2002.

[7] E. Coetzee, B. Krauskopf, and M. Lowenberg. Application of bifurcation methods for the prediction of low-speed aircraft ground performance. *Journal of Aircraft*, 47(4):1248–1255, 2010.

[8] E. Coetzee, B. Krauskopf, and M. Lowenberg. Analysis of medium-speed runway exit manoeuvres. *Journal of Aircraft*, 48(5):1553–1564, 2011.

[9] M. Dengler, M. Goland, and G. Herrman. A bibliographic survey of automobile and aircraft wheel shimmy. Technical report, WADC 52-141, Midwest Research Institute, Kansas City, MO, USA, 1951.

[10] J. Dennis. Analytical investigation of damping of landing gear shimmy. In *Proceedings of the SAE Aerospace Technology Conference and Exposition*, Long Beach, CA, October 1-4 1990.

[11] E. J. Doedel, with major contributions from A. R. Champneys, T. F. Fairgrieve, Yu. A. Kuznetsov, B. E. Oldeman, R. C. Paffenroth, B. Sandstede, X. J. Wang, and C. Zhang. Auto-07P: Continuation and bifurcation software for ordinary differential equations. Concordia University, Montreal, Canada, 2008; available at `http://cmvl.cs.concordia.ca/`.

[12] H. Erzgräber, B. Krauskopf, and D. Lenstra. Bifurcation analysis of a semiconductor laser with filtered optical feedback. *SIAM Journal on Applied Dynamical Systems*, 6:1–28, 2007.

[13] J. Glaser and G. Hrycko. Landing gear shimmy - de Havilland's experience. *AGARD-R-800*, 1996.

[14] K. Green and B. Krauskopf. Bifurcation analysis of a semiconductor laser subject to non-instantaneous phase-conjugate. *Optics Communications*, 231:383–393, 2004.

[15] D. Grossman. F-15 nose landing gear shimmy, taxi test and correlative analyses. *SAE Paper 801239*, 1980.

[16] B. Krauskopf and J. Walker. Bifurcation study of a semiconductor laser with saturable absorber and delayed optical feedback. In K. Lüdge, editor, *Nonlinear Laser Dynamics. From Quantum Dots toCryptography*, pages 161–181. Wiley-VCH, 2012.

[17] G. Li. Modelling and analysis of a dual-wheel nose gear: shimmy instability and impact motions. In *Proceedings of the SAE Aerospace Atlantic Conference and Exposition*, Dayton, Ohio, April 20-23 1993.

[18] M.L Lowenberg, D. Rezgui, and P. Bunness. Experimental evaluation of numerical continuation and bifurcation methods applied to autogyro rotor blade aeromechanical stability *Proceedings of ASME DETC/CIE2009*, DETC2009-87634, 379–387, 2009.

[19] E. Maier and M. Renz. Tests on shimmy with the nose landing gear of the Me 309 and the FKFS trailer. N-579 AAF, Air Material Command, Wright Field Technical Intelligence, Dayton, Ohio, 1947.

[20] W. Moreland. Landing gear vibration. *A. F. tech. Rep.*, 6590, 1951.

[21] J. Pritchard. An overview of landing gear dynamics. Technical report, NASA/TM-1999-209143, 1999.

[22] J. Rankin, M. Desroches, B. Krauskopf, and M. Lowenberg. Canard cycles in aircraft ground dynamics. *Nonlinear Dynamics*, 66(4):681–688, 2011.

[23] J. Rankin, B. Krauskopf, M. Lowenberg, and E. Coetzee. Nonlinear analysis of lateral loading during taxiway turns. *Journal of Guidance, Control, and Dynamics*, 33(6):1708–1717, 2010.

[24] J. Rankin, B. Krauskopf, M. Lowenberg, and E. Coetzee. Operational parameter study of aircraft dynamics on the ground. *Journal of Computational and Nonlinear Dynamics*, 5(2):021007, 2010.

[25] J. Rotta. Mathematical analysis of wheel shimmy (in German). *FW-ROT-21-9-44*, CADO no. 66 5241-4, 1944.

[26] D. Sensaud de Lavaud. Shimmy, pseudo-shimmy and tramp of an automobile (in French). *C. R. Acad. Sci. Paris*, 185:254–257, 1927.

[27] D. Sensaud de Lavaud. The fundamental critical speeds of automobiles (in French). *C. R. Acad. Sci. Paris*, 184:1636–1638, 1927.

[28] D. Sensaud de Lavaud. Independently sprung front wheels a remedy for shimmy. *Soc. auto.Engrs*, 22:623–635, 1928.

[29] G. Somieski. Shimmy analysis of a simple aircraft nose landing gear model using different mathematical methods. *Aerospace Science and Technology*, 8:545–555, 1997.

[30] G. Temple. Large angle shimmy. *Roy. Aircr. Establ.*, ATI no. 40738, 1941.

[31] P. Thota, B. Krauskopf, and M. Lowenberg. Interaction of torsion and lateral bending in aircraft nose landing gear shimmy. *Nonlinear Dynamics*, 57(3):455–467, 2009.

[32] P. Thota, B. Krauskopf, and M. Lowenberg. Bifurcation analysis of nose landing gear shimmy with lateral and longitudinal bending. *Journal of Aircraft*, 47(1):87–95, 2010.

[33] P. Thota, B. Krauskopf, and M. Lowenberg. Multi-parameter bifurcation study of shimmy oscillation in a dual-wheel aircraft nose landing gear. Technical report, University of Bristol, 2011. BCANM.1786.

[34] R. Van Der Valk and H. Pacejka. An analysis of a civil aircraft main gear shimmy failure. *Vehicle System Dynamics*, 22(2):97–121, 1993.

[35] B. von Schlippe and R. Dietrich. Shimmying of a pneumatic wheel. Technical report, NACA TM 1365, 1947.

[36] P. Woerner and O. Noel. Influence of nonlinearity on the shimmy behaviour of landing gear. *R-800*, 1995.

[37] D. Yadov and R. Ramamoorthy. Nonlinear landing gear behaviour at touchdown. *Journal of Dynamical Systems, Measurement, and Control*, 113:677–683, 1991.